www.the-innovation.org

Schottky infrared detectors with optically tunable barriers beyond the internal photoemission limit

Jintao Fu,[1,2] Zhongmin Guo,[1,2] Changbin Nie,[1,2] Feiying Sun,[1] Genglin Li,[1,2] Shuanglong Feng,[1,2,3] and Xingzhan Wei[1,2,3,*]

*Correspondence: weixingzhan@cigit.ac.cn

Received: September 16, 2023; Accepted: February 27, 2024; Published Online: February 29, 2024; https://doi.org/10.1016/j.xinn.2024.100600

© 2024 The Authors. This is an open access article under the CC BY-NC-ND license (http://creativecommons.org/licenses/by-nc-nd/4.0/).

GRAPHICAL ABSTRACT

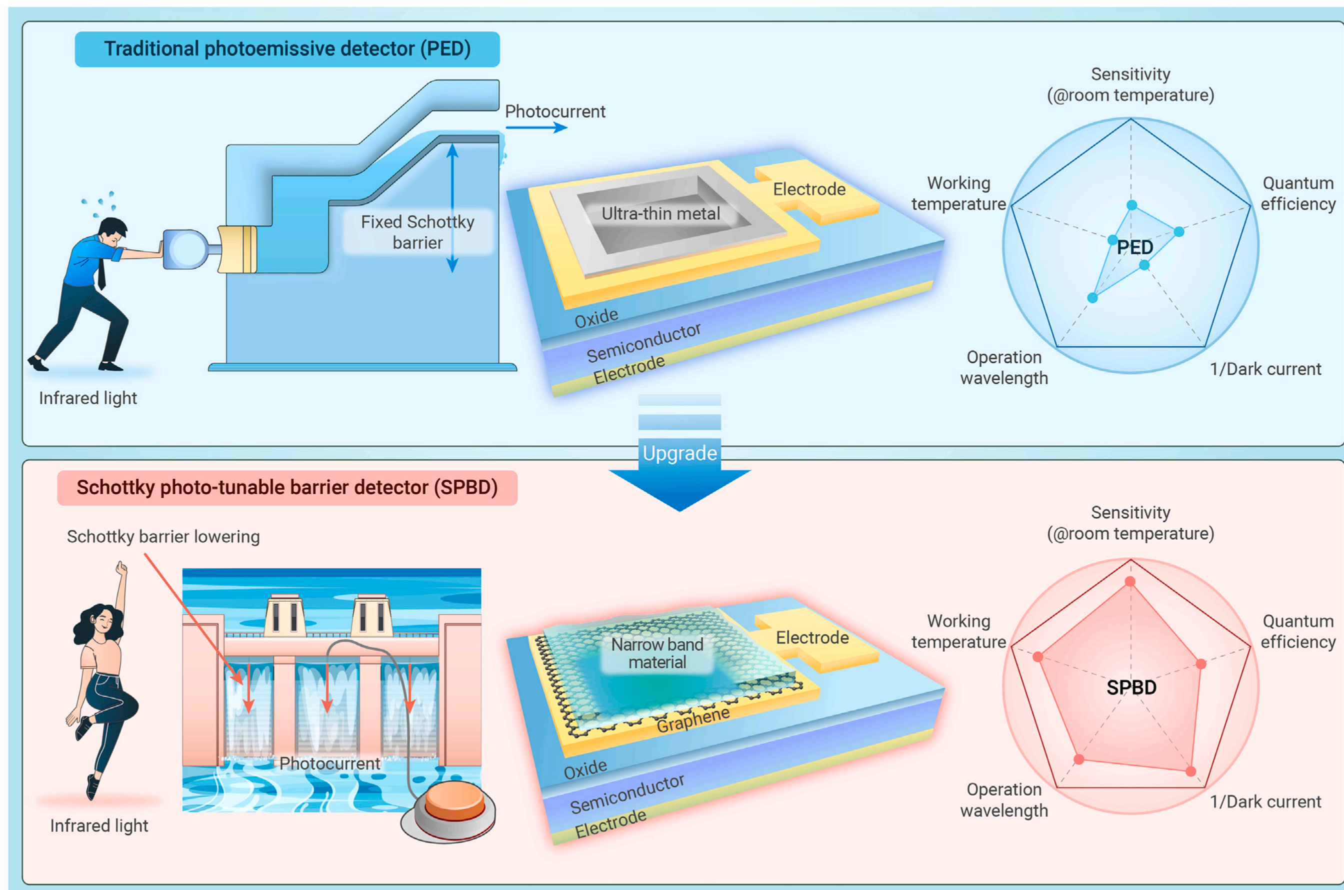

PUBLIC SUMMARY

- An infrared detector with an optically tunable barrier is proposed to overcome the internal photoemission limit.
- Broadband infrared detection is attained while maintaining a low dark current.
- Highly sensitive blackbody radiation sensing is achieved at room temperature.
- This strategy shows promise for realizing uncooled, high-performance silicon-based infrared sensors.

Schottky infrared detectors with optically tunable barriers beyond the internal photoemission limit

Jintao Fu,[1,2] Zhongmin Guo,[1,2] Changbin Nie,[1,2] Feiying Sun,[1] Genglin Li,[1,2] Shuanglong Feng,[1,2,3] and Xingzhan Wei[1,2,3,*]

[1]Chongqing Institute of Green and Intelligent Technology, Chinese Academy of Sciences, Chongqing 400714, China

[2]University of Chinese Academy of Sciences, Beijing 100049, China

[3]Chongqing School, University of Chinese Academy of Sciences, Chongqing 400714, China

*Correspondence: weixingzhan@cigit.ac.cn

Received: September 16, 2023; Accepted: February 27, 2024; Published Online: February 29, 2024; https://doi.org/10.1016/j.xinn.2024.100600

© 2024 The Authors. This is an open access article under the CC BY-NC-ND license (http://creativecommons.org/licenses/by-nc-nd/4.0/).

Citation: Fu J., Guo Z., Nie C., et al., (2024). Schottky infrared detectors with optically tunable barriers beyond the internal photoemission limit. The Innovation **5(3)**, 100600.

Internal photoemission is a prominent branch of the photoelectric effect and has emerged as a viable method for detecting photons with energies below the semiconductor bandgap. This breakthrough has played a significant role in accelerating the development of infrared imaging in one chip with state-of-the-art silicon techniques. However, the performance of these Schottky infrared detectors is currently hindered by the limit of internal photoemission; specifically, a low Schottky barrier height is inevitable for the detection of low-energy infrared photons. Herein, a distinct paradigm of Schottky infrared detectors is proposed to overcome the internal photoemission limit by introducing an optically tunable barrier. This device uses an infrared absorbing material-sensitized Schottky diode, assisted by the highly adjustable Fermi level of graphene, which subtly decouples the photon energy from the Schottky barrier height. Correspondingly, a broadband photoresponse spanning from ultraviolet to mid-wave infrared is achieved, with a high specific detectivity of 9.83×10^{10} cm Hz$^{1/2}$ W^{-1} at 2,700 nm and an excellent specific detectivity of 7.2×10^{9} cm Hz$^{1/2}$ W^{-1} at room temperature under blackbody radiation. These results address a key challenge in internal photoemission and hold great promise for the development of the Schottky infrared detector with high sensitivity and room temperature operation.

INTRODUCTION

Schottky infrared detectors (also known as photoemissive detectors) are assembled from metals and semiconductors and possess the unique advantages of broadband photoresponse, high uniformity, and full compatibility with complementary metal oxide semiconductor (CMOS) technology in the field of infrared detection. However, Schottky infrared detectors generally have a trade-off between the quantum efficiency and cutoff wavelength against the dark current.[1,2] This trade-off is related to the limit of internal photoemission, which originates from the association between the Schottky barrier height and photon energy. Specifically, internal photoemission enables the Schottky infrared detectors to sense infrared photons with energies lower than the bandgap of the semiconductor. However, as the infrared photon energy decreases, the blocking effect of the Schottky barrier on the photoemission of hot carriers becomes evident, which greatly degrades the detection capability of the Schottky infrared detectors.[3] Although lowering the barrier can extend the cutoff wavelength and increase the quantum efficiency, the dark current will also dramatically increase,[4,5] causing a severe decrease in detectivity; detectivity is a figure of merit for evaluating the sensitivity of photodetectors.[6] As a compromise, cryogenic cooling systems are generally utilized;[7] however, they are bulky, heavy, and inconvenient to use.

A promising way to improve the performance of Schottky infrared detectors is to strengthen optical absorption by introducing microcavities,[8] waveguides,[9] metallic nanoantennas,[10] surface plasmon polaritons,[11,12] and light-trapping structures.[13] In an alternative approach, emerging two-dimensional materials, such as graphene, with intriguing linear energy-momentum relationships, have been utilized to replace metals to increase the probability of hot carrier emission.[14,15] Moreover, by physically laminating metal with an atomically flat surface onto a dangling-band-free two-dimensional material, an ideal Schottky interface can be obtained to achieve efficient internal photoemission.[16] These methods have successfully promoted the photoresponse of the Schottky infrared detectors within the near-infrared range. Nevertheless, the solution to overcome the limit of internal photoemission remains elusive; thus, the detection of longer wavelengths with high sensitivity at room temperature remains challenging.

In this study, an uncooled Schottky photo-tunable barrier detector (SPBD) is proposed to overcome the internal photoemission limit, enabling broadband and highly sensitive photodetection capabilities. The SPBD configuration contains a graphene-silicon (Gra-Si) Schottky junction for carrier blocking and a narrow bandgap lead telluride (PbTe) for infrared light absorption. Essentially different from that of conventional Schottky infrared detectors, the photoresponse of the SPBD originates from the variation in the Schottky barrier under infrared illumination. Moreover, a large Schottky barrier can be maintained to suppress the dark currents. As a result, infrared light with photon energy below the barrier can be detected without sacrificing detectivity. Experimentally, the SPBD exhibits broadband detection (254–4,000 nm), a low dark current density ($<10^{-3}$ A/cm^2), and a fast response speed (0.13 ms/0.11 ms). More importantly, the device possesses a room-temperature specific detectivity of up to 7.2×10^{9} cm Hz$^{1/2}$ W^{-1} under blackbody radiation, which is a reliable approach for gauging the performance of infrared photodetectors by imitating realistic objects.[17]

RESULTS

Device working mechanism and structure

Figures 1A and 1B display the operation mechanism of the SPBD in comparison with that of a typical photoemission detector. The photoresponse of a photoemissive detector is dominated by internal photoemission. Specifically, the hot electrons excited by high-energy photons in a metal can be injected over the Schottky barrier to generate a photocurrent. However, a photoemissive detector can hardly detect illumination with a photon energy lower than the Schottky barrier height (SBH) because the hot electrons excited by low-energy photons have difficulty crossing the barrier. Although the utilization of a low SBH can solve this issue, a low SBH inevitably leads to a large dark current. The optically tunable barrier of the SPBD contributes to the photoresponse. Specifically, the electrons excited by infrared light in the narrow bandgap material are injected into graphene, causing the Fermi level of graphene to increase (Section S1). As a result, the SBH of the SPBD is optically reduced, and a measurable photocurrent is obtained. This process successfully decouples the photon energy from the SBH, which allows the SPBD to utilize a large SBH to suppress the dark current and detect infrared light with photon energies below the SBH.

According to the analysis models of the photoemission detector and SPBD (Section S2), the SPBD can maintain a lower dark current than a photoemissive detector operating at room temperature or even under cryogenic conditions by exploiting the large SBH (Figure 1C). Furthermore, with decreasing photon energy, the energy of the hot electrons decreases, leading to fewer hot electrons being emitted across the barrier in the photoemissive detector. Thus, the external quantum efficiency (EQE) of the photoemissive detector continues to decrease with increasing light wavelength. For the SPBD, the decrease in the SBH under illumination enables a large number of electrons to cross the barrier, which results in a relatively high EQE compared with that of the photoemissive detector (Figure 1D).

The structure schematic, transmission electron microscopy (TEM), and optical microscope images of the SPBD are shown in Figures 1E, S2, and S3A inset, respectively. The monolayer graphene (see Raman spectral in Figure S3A) is attached to lightly n-doped Si to form a Schottky junction with van der Waals contact. PbTe is an infrared photosensitive layer and covers the surface of graphene. Photocurrent mapping (Figure S3B) indicates that the photocurrent mainly flows through the overlapping area of graphene and Si. According to the experimentally measured I–V curves (Figure 1F), the SPBD exhibits a strong rectifying behavior, and its dark current density is within 10^{-3} A/cm^2. In addition, due to the

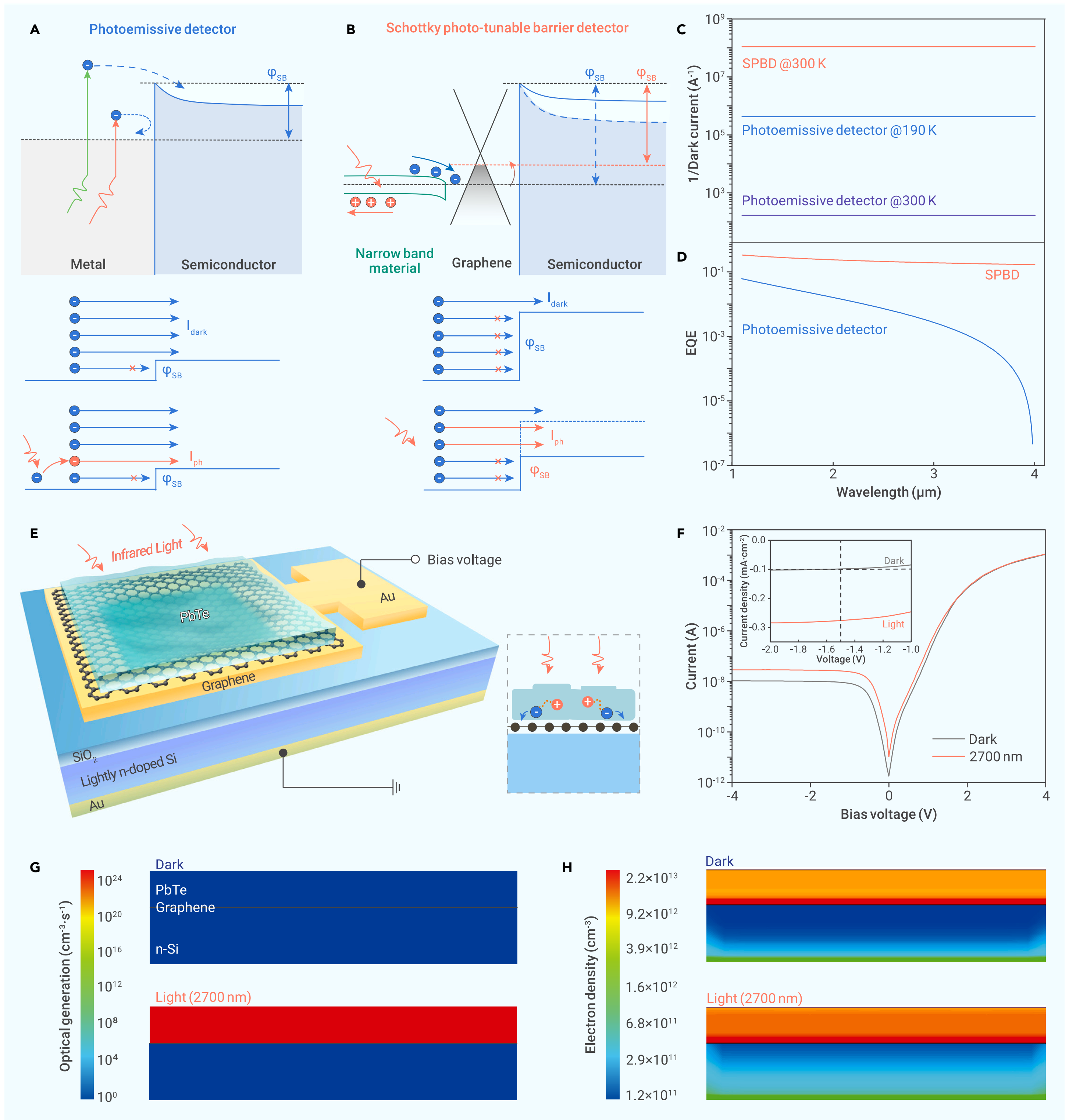

Figure 1. Conception and characteristics of the SPBD Working mechanism illustration of a (A) typical photoemissive detector with a metal-semiconductor junction and the (B) proposed SPBD herein. φ_{SB}, I_{dark}, and I_{ph} indicate the Schottky barrier height, dark current, and photocurrent, respectively. The green (red) wavy arrow represents light with high (low) photon energy. (C) Dark current as a function of the wavelength for the photoemissive detector and SPBD. Since the dark current is related to φ_{SB}, temperature, and bias voltage, the dark current is consistent under different wavelengths of light. (D) EQE vs. wavelength plots for the photoemissive detector and SPBD. The spectral response of the narrow bandgap material in the analysis model is assumed to be wavelength-independent. (E) Schematic diagram of the SPBD. Infrared light excites electron-hole pairs in PbTe. The photogenerated electrons will be injected into graphene, increasing the Fermi level of graphene. (F) I–V curves of the SPBD in the dark and under 2,700 nm illumination. Smooth I–V curves imply good contact between the top Au layer and graphene, as well as between the bottom Au layer and Si. The increase in current under infrared illumination can be attributed to the decrease in the SBH. However, as the Gra-Si junction is gradually forward-biased, a substantial increase in forward current dominates, overshadowing the incremental current caused by infrared light. (G and H) Simulated optical generation and electron density profile under 2,700 nm illumination compared with the equilibrium in the dark.

introduction of PbTe, the SPBD responds to 2,700 nm light, which is impossible for bare Si detectors. Note that the photon energy of 2,700 nm light (0.46 eV) is lower than the SBH (0.658 eV, see Figure S4) in the SPBD; this result indicates that the photoresponse of the SPBD originates from an optically lowered barrier.

In addition, the capacitance-voltage measurements demonstrate a decrease in the SBH of the SPBD under 2,700 nm illumination compared with that under the dark condition (Section S5). This decreased SBH can also be viewed as a result of the photo-induced doping, along with other impressive two-dimensional

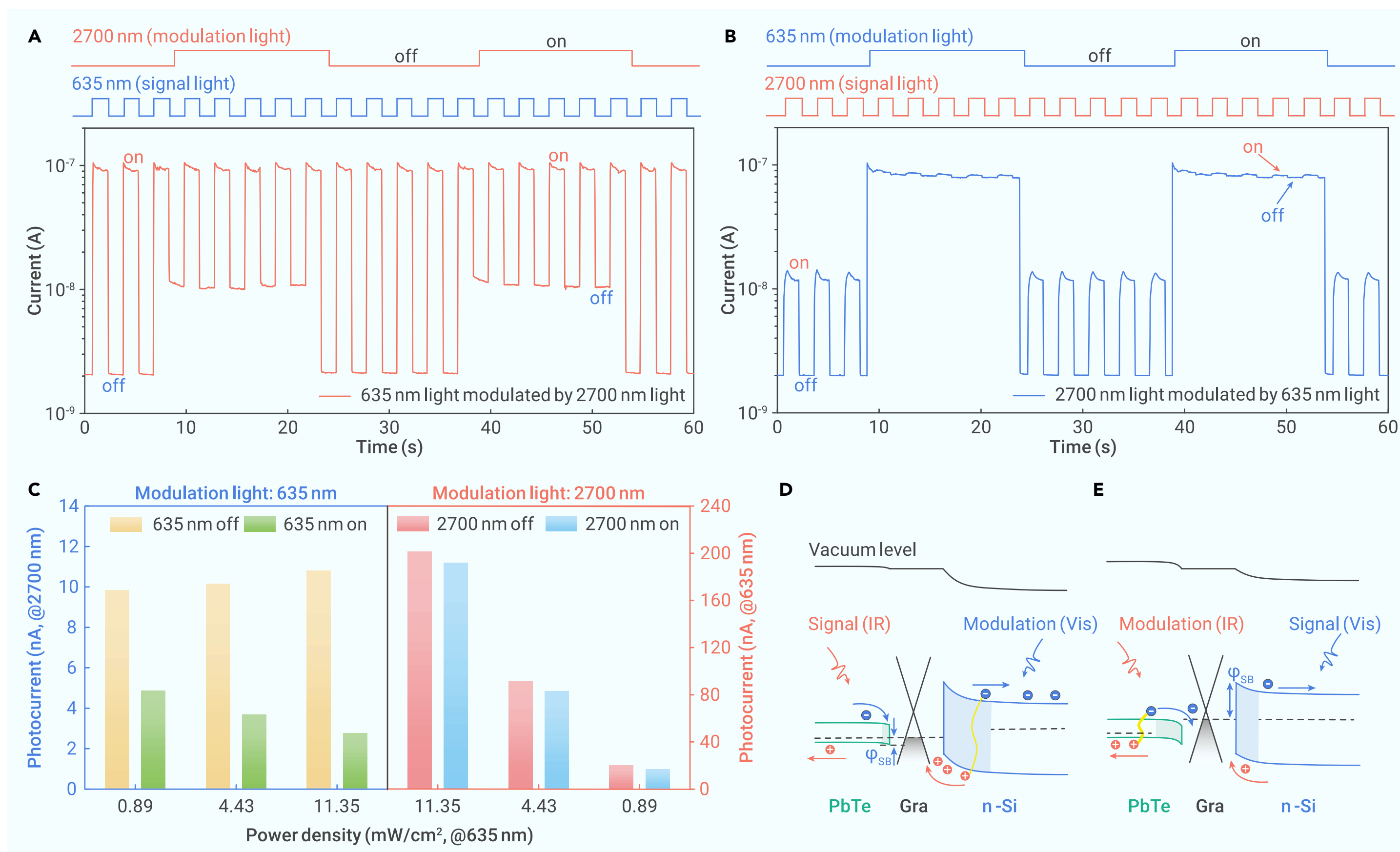

Figure 2. Effect of graphene Fermi level variation on the photocurrent Time-dependent current response when the Vis (A) and SWIR (B) lights act as the modulation sources. The power densities of the 2,700 nm and 635 nm lasers are 119 mW/cm^2 and 4.43 mW/cm^2, respectively. (C) Net photocurrent of the SPBD under different modulation conditions. (D and E) Energy band diagrams corresponding to the situations in (A) and (B), respectively. Since the quantum efficiency of PbTe is extremely weak near and below 1.5 μm,[22] the carriers excited by Vis light in PbTe are assumed to be negligible.

material doping approaches;[18–21] these doping approaches promote the photodetection capabilities of the devices.

Using computer-aided design software (Section S6), the working principle of the SPBD is illustrated. Figure 1G shows the optical generation inside the SPBD; here, the carriers induced by infrared light are mainly generated within PbTe. As the photogenerated electrons move toward graphene, the electron density near the PbTe-Gra junction increases (Figure 1H). Subsequently, the reduced Schottky barrier in the Gra-Si junction region causes more electrons to cross the barrier and enter Si. Therefore, the electron density in Si also increases, which produces a photocurrent under infrared illumination.

Verification of the device working mechanism

To further verify the working principle, an experimental scheme is designed to introduce visible light (Vis, 635 nm) and short-wave infrared light (SWIR, 2700 nm) to excite the photogenerated carriers in Si and PbTe, respectively. By using these two light sources to modulate each other, the optically modulated currents are recorded (Figures 2A, 2B, and S6). During this process, the carriers excited by the modulation light are injected into graphene, which tunes the Fermi level of graphene. Subsequently, the variation in the Fermi level alters the junction characteristics, such as the SBH, build-in field, and depletion region width (Section S8), and ultimately modulates the photocurrent excited by the signal light.

Figure 2C shows the net photocurrent under different optical modulation conditions. Regardless of which light source is used for modulation, the signal photocurrent decreases. Typically, the photocurrents generated by two light sources are superimposed (within the linear dynamic range) for conventional photodetectors, while the opposite occurs for SPBD. This result can be explained as follows. When Vis light is used as the modulation light (Figure 2D), it can excite a large number of electron-hole pairs in Si. Driven by the built-in field in the Gra-Si junction, the photogenerated holes are injected into graphene, leading to a decrease in the Fermi level of graphene.[23,24] Compared with Si, PbTe remains almost in a steady state; therefore, the PbTe-Gra junction can be analyzed according to the Schottky junction model. When the graphene Fermi level decreases, the built-in field of the PbTe-Gra junction weakens, resulting in the contraction of the depletion layer. Consequently, the separation efficiency of the photogenerated carriers in the PbTe-Gra junction decreases, and the SWIR photocurrent decreases.

In contrast, when SWIR is used as the modulation light (Figure 2E), the photogenerated electrons in PbTe are injected into graphene, increasing the graphene Fermi level. Since Si is in a steady state, the increase in the graphene Fermi level leads to a decrease in the Schottky barrier in the Gra-Si junction, as well as a decrease in the built-in field and the width of the depletion region. As a result, the Vis photocurrent is reduced. Thus, the photoresponse is presumed to mainly originate from the Schottky barrier variation caused by the shift of the graphene Fermi level under illumination.

Broadband photodetection

Next, the broadband photodetection capacity of the SPBD is tested. In addition to ultraviolet (UV) (254 nm, Figures S7A and S7B) and Vis (365 nm, Figures S7C and S7D; 635 nm, Figure 3A) light, the device is sensitive to near-infrared (NIR) (1,550 nm, Figure S8), SWIR (2,700 nm, Figure 3B), and middle wavelength infrared (MWIR) (4,000 nm, Figure S9) light. Furthermore, the SPBD shows notable long-term stability, with a slight degradation in the photoresponse after 1 year (Section S10). To analyze the laser response performance of the SPBD, its responsivity and EQE are calculated and plotted in Figures 3C and S10. The highest responsivity and EQE are 464 mA/W and 90%, respectively, in the Vis region; these values are comparable to those of previously reported high-performance photodetectors based on graphene and organic films.[25,26] More importantly, the device has a responsivity of 50 mA/W and an EQE of 2.5% in the SWIR region at room temperature; these results are comparable or even superior to those of the classical PtSi photoemissive photodetector in a cryogenic cooling environment.[7,27,28] The photovoltage response of the SPBD in the SWIR region is

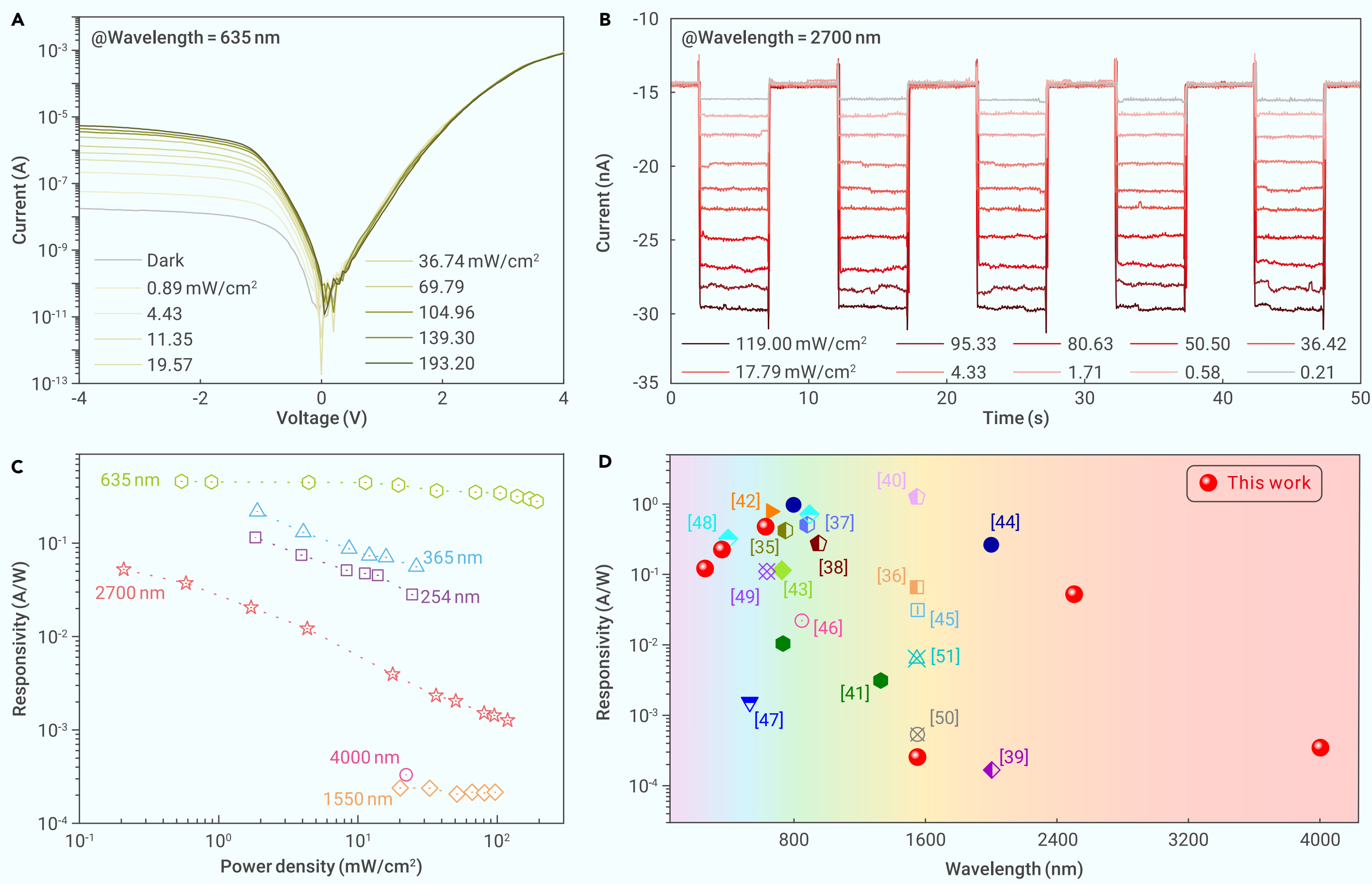

Figure 3. Broadband response of the SPBD (A and B) Photoresponse characteristics of the SPBD under Vis (635 nm) and SWIR (2,700 nm) light illumination. (C) Responsivity vs. power density under different light wavelengths. (D) Performance of the SPBD and other reported graphene-based photodetectors.

also measured (Figure S11); here, the highest voltage responsivity and specific detectivity reaches 10^6 V/W and 9.83×10^{10} cm Hz$^{1/2}$ W^{-1}, respectively. The remarkable specific detectivity exhibited by the SPBD is attributed to its working mechanism, which exceeds the limit of internal photoemission. A high SBH effectively mitigates the dark current, while an optically tunable SBH results in a substantial infrared photoresponse. Notably, alongside ingenious heterojunction engineering,[29–34] the operational mechanism of the SPBD provides an alternative approach for reducing the dark current while enhancing the photoresponse, which shows great potential for achieving highly sensitive infrared photodetection. To further evaluate its broadband detection ability, the SPBD is compared with other graphene-based photodetectors[35–51] (Table S4). The SPBD not only has a responsivity comparable to those of these other devices in the UV−Vis region but also possesses a detectable wavelength region from the UV to the MWIR, as shown in Figure 3D.

Blackbody sensitivity

Blackbody radiation closely simulates the emission characteristics of realistic objects and is commonly employed to evaluate the practical performance of infrared photodetectors;[17] thus, the blackbody detection performance of the SPBD at room temperature is specifically examined. A schematic diagram of the measurement system is shown in Figure S13A. The photovoltage response of the SPBD under blackbody radiation at different temperatures is shown in Figure 4A. As the blackbody temperature increases, the radiation power increases (Figure S13B), and the peak wavelength blueshifts (Figure S13C), resulting in an increase in the photovoltage. The current response of the SPBD under blackbody radiation is also measured (Figure S14) and shows a trend similar to that of the voltage response. Figure 4B displays the noise voltage variation, and the 1/f noise behavior is prominent at low frequencies; this result is consistent with the previously reported Gra-Si photodiode.[52] In addition, due to the bias voltage, random telegraph noise is superimposed on the 1/f noise, causing the noise voltage curve to bulge.[53] Figure 4C shows the specific detectivity and equivalent noise power (NEP) of the SPBD. The highest specific detectivity and the lowest NEP are 7.2×10^9 cm Hz$^{1/2}$ W^{-1} and 1.4×10^{-12} W Hz$^{-1/2}$, respectively; these results are comparable to those of blackbody sensitive detectors based on low-dimensional materials.[54,55] Moreover, due to the low dark current, even under 500 K blackbody radiation at room temperature, the device still achieves a specific detectivity of 7.0×10^8 cm Hz$^{1/2}$ W^{-1}.

Subsequently, by exploiting a 2,700 nm laser modulated at high frequency as a light source, the temporal response of the SPBD is characterized. The rising time and falling time, defined as the time necessary for the net photocurrent to increase from 10% to 90% and decrease from 90% to 10%, are 0.13 ms and 0.11 ms (Figures 4D and 4E), respectively. By reducing the thickness of the Si substrate or designing a PIN-like doping profile, the response speed of the SPBD is expected to further improve.

Photoresponse of the SPBD array

Finally, the photoresponse of the SPBD array is measured. By using a custom mask to block part of the light, a 5×5 SPBD array is used to detect the corresponding spot pattern (Figure 5A, top panel). An image of the 5×5 SPBD array and schematic diagrams of two custom masks representing the English letters "C" and "Q" are shown in the bottom panel of Figure 5A. Upon blackbody radiation, the pixels under the exposed area produce evident photocurrents, while the photocurrents recorded from pixels under the blocked area are negligible. The photocurrents obtained in all pixels are shown in Figures 5B and 5C; here, the corresponding shape letters "C" and "Q" can be recognized. These results indicate that the SPBD should have great potential for imaging applications.

CONCLUSION

In summary, an intriguing device architecture with low dark current, broadband photodetection, high response speed, and blackbody sensitivity at room

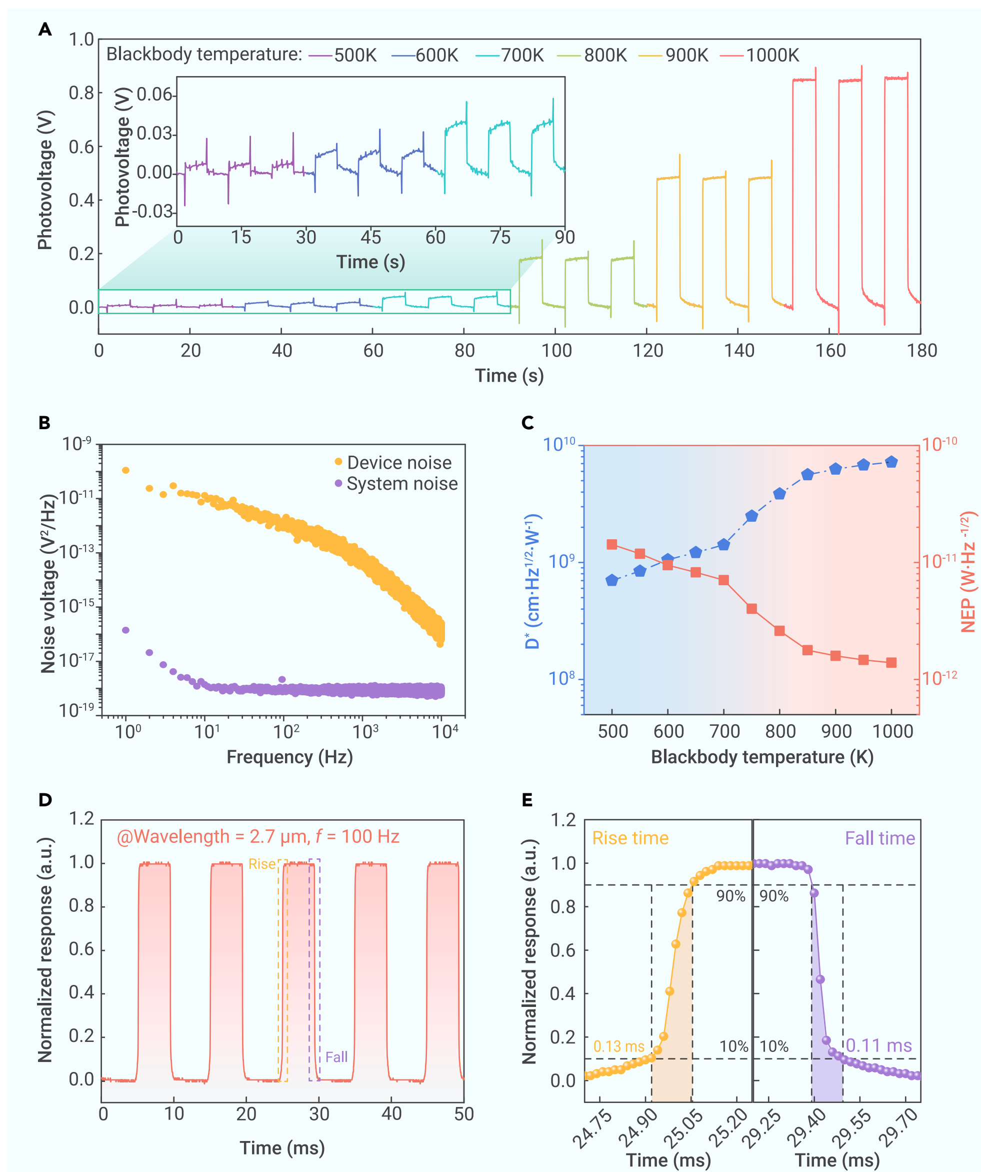

Figure 4. Blackbody sensitivity, noise, and response speed of the SPBD (A) Time-dependent photovoltage response under blackbody radiation at different temperatures. The bias current is −10 nA. (B) Noise voltage of the device and the system. The noise voltage of the device at 1 kHz is 6.47×10^{-14} V^2/Hz. (C) Specific detectivity and NEP of the device with different blackbody temperatures. (D) Temporal response of the device. (E) Close-ups of the rising and falling edges (indicated by the shaded boxed regions in D).

temperature is proposed and demonstrated. A conventional photoemissive detector based on a metal-semiconductor Schottky junction requires a barrier height below the photon energy; however, the SPBD provides an effective way to achieve a wide detectable wavelength and a low conduction dark current by decoupling the infrared photon energy and SBH. The SPBD is highly important for attaining inexpensive, low-power consumption Si-based infrared sensors. More significantly, the performance could be further improved by substituting the original infrared sensitizer with emerging materials[56] and optimizing the graphene transfer technology,[57] thereby enhancing the quality of the Schottky junction.

MATERIALS AND METHODS

Electrochemical growth of PbTe

PbTe was deposited on the surface of a SiO_2/Si substrate covered with an Au film by electrochemical growth. Cyclic voltammetry and coulometry experiments were performed using a CH310H electrochemical workstation. A common three-electrode cell including a working electrode, counter electrode, and reference electrode was used to apply and read voltages by connecting with the electrochemical workstation. The working electrode was connected to a SiO_2/Si substrate, while platinum foil and Ag/AgCl were used as the counter electrode and reference electrode, respectively. The electrolyte solution used in the experiment was prepared with deionized water. The electrochemical deposition of PbTe was conducted in a mixed solution containing 5 mM $Pb(NO_3)_2$ (>99%) dissolved in 100 mM NaOH (98%) and 10 mM TeO_2 (>99.99%) dissolved in 100 mM NaOH. Finally, the electrochemically grown PbTe was dispersed from the substrate to ethanol by ultrasonic vibration to produce the PbTe dispersion solution.[58]

Material characterization

Section S13 shows the characteristics of PbTe. The phase of PbTe was identified by X-ray diffraction using a D8 ADVANCE instrument. The morphology, crystal structure, and crystallinity of PbTe were characterized by using TEM (Tecnai G2 F30 S-Twin) and high-resolution TEM. X-ray photoelectron spectroscopy was performed with a Thermo ESCALAB 250Xi instrument to analyze the elemental composition and chemical state of PbTe. The Raman spectra were measured to evaluate the quality of the graphene by using a Renishaw inVia Reflex instrument, and the laser excitation wavelength was 532 nm.

SPBD fabrication

Section S14 shows the fabrication process diagram of PbTe. The SPBD was fabricated on a lightly n-doped Si substrate (resistivity 5–10 Ω cm, thickness 500 μm) with a 300-nm SiO_2 layer. The electrodes (50 nm Au) were prepared by photolithography and magnetron sputtering, with a lift-off process. SiO_2 windows were defined by photolithography, and the substrate was then immersed in an etching solution (BOE:H_2O = 1:1) for 210 s to remove SiO_2 and expose Si. After wet etching, the substrate was successively immersed in deionized water and acetone to remove the etching solution and photoresist. The CVD-grown monolayer graphene was subsequently transferred onto the substrate by polymethyl methacrylate (PMMA)-assisted wet transfer technology. The substrate was dried for 12 h and then heated at 150°C for 40 min to promote the adhesion of graphene and Si. Next, acetone was used to remove the PMMA. Next, graphene was patterned by photolithography and oxygen plasmon etching. The PbTe dispersion solution was added dropwise on the substrate surface, followed by spinning at 500 rpm for 5 s. The substrate was dried ethanol at 80°C and heated at 150°C; afterward, the contact between these materials was optimized. The fabrication process of the 5 × 5 device array is the same as that of the single-point SPBD.

Device performance measurements

The electrical characteristics of the SPBDs were measured by a Keithley 4200-scs semiconductor analyzer. The capacitance measurements were performed using a small AC signal amplitude of 25 mV at an 8 kHz frequency superimposed on a DC bias voltage, which was swept from −4 to 4 V. The photocurrent mapping was obtained by scanning over the device using a scanning Galvo System (Thorlabs GVS212) with a focused 980 nm laser beam (spot diameter of ∼2 μm). For the broadband photodetection test, a UV light-emitting diode (LED) with 254 nm and 365 nm filters and four lasers with emission of 635 nm, 1,550 nm, 2,700 nm, and 4,000 nm were used as light sources. A low-frequency modulated light signal was generated by using an electronic shutter (GCI-73M, Daheng Optics). The power of the light source was calibrated by using a commercial optical power meter (Thorlabs S405C). The response speed of the device was measured by switching the 2,700 nm laser on and off with a signal generator (RIGOL DG1022U) and recorded by an oscilloscope (Tektronix DPO 5204). The blackbody test was conducted by using a commercial blackbody radiation source (SR 200N). The noise of the device was measured by a noise spectrum

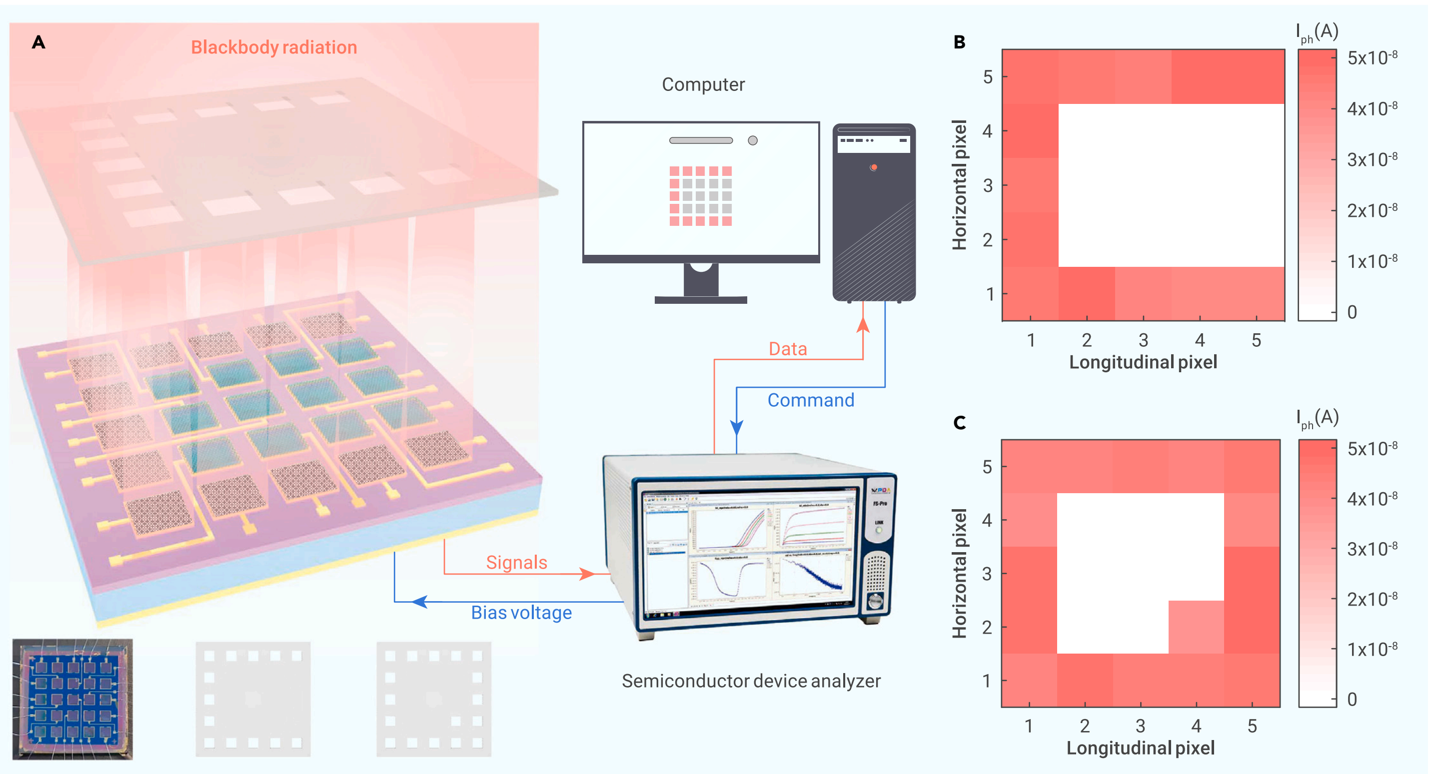

Figure 5. Photoresponse of the SPBD array (A) Top: schematic of the photoresponse measurement based on the device array. Bottom: photograph of the 5 × 5 device array and the schematics of the two custom masks representing "C" and "Q." The photosensitive area of each pixel is 1 mm × 1 mm. The results of the letter pattern when using masks (B) "C" and (C) "Q" under 1,000 K blackbody radiation. The photoresponse of the SPBD array when using a light-emitting diode (LED) as a light source is shown in Figure S15, which exhibits similar results.

analyzer (Shenzhen Liangwei Co., Ltd.). The light sources used for measuring the photoresponse of the device array were a blackbody with 1,000 K and an ordinary white LED lamp.

REFERENCES

1. Casalino, M. (2016). Internal Photoemission Theory: Comments and Theoretical Limitations on the Performance of Near-Infrared Silicon Schottky Photodetectors. IEEE J. Quant. Electron. **52**(4): 1–10. https://doi.org/10.1109/jqe.2016.2532866.
2. Scales, C., and Berini, P. (2010). Thin-Film Schottky Barrier Photodetector Models. IEEE J. Quant. Electron. **46**(5): 633–643. https://doi.org/10.1109/jqe.2010.2046720.
3. Massicotte, M., Schmidt, P., Vialla, F., et al. (2016). Photo-thermionic effect in vertical graphene heterostructures. Nat. Commun. **7**: 12174. https://doi.org/10.1038/ncomms12174.
4. Rogalski, A. (2000). Infrared Detectors (CRC press).
5. Brongersma, M.L., Halas, N.J., and Nordlander, P. (2015). Plasmon-induced hot carrier science and technology. Nat. Nanotechnol. **10**(1): 25–34. https://doi.org/10.1038/nnano.2014.311.
6. Zhao, W., Yan, Y., Chen, X., et al. (2022). Combining printing and nanoparticle assembly: Methodology and application of nanoparticle patterning. Innovation **3**(4): 100253. https://doi.org/10.1016/j.xinn.2022.100253.
7. Wang, W.S., Ho, C., and Chuang, T.M. (1998). High-performance IR Detectors Fabricated by PtSi on P-Si Substrate. In Infrared Detectors and Focal Plane Arrays V.
8. Casalino, M., Sirleto, L., Moretti, L., et al. (2009). Back-illuminated silicon resonant cavity-enhanced photodetector at 1550 nm. Phys. E Low-dimens. Syst. Nanostruct. **41**(6): 1097–1101. https://doi.org/10.1016/j.physe.2008.08.049.
9. Zhu, S., Yu, M.B., Lo, G.Q., et al. (2008). Near-infrared waveguide-based nickel silicide Schottky-barrier photodetector for optical communications. Appl. Phys. Lett. **92**(8): 081103. https://doi.org/10.1063/1.2885089.
10. Knight, M.W., Sobhani, H., Nordlander, P., et al. (2011). Photodetection with Active Optical Antennas. Science **332**(6030): 702–704. https://doi.org/10.1126/science.1203056.
11. Akbari, A., Tait, R.N., and Berini, P. (2010). Surface plasmon waveguide Schottky detector. Opt Express **18**(8): 8505–8514. https://doi.org/10.1364/OE.18.008505.
12. Desiatov, B., Goykhman, I., Mazurski, N., et al. (2015). Plasmonic enhanced silicon pyramids for internal photoemission Schottky detectors in the near-infrared regime. Optica **2**(4): 335–338. https://doi.org/10.1364/optica.2.000335.
13. Steglich, M., Zilk, M., Bingel, A., et al. (2013). A normal-incidence PtSi photoemissive detector with black silicon light-trapping. J. Appl. Phys. **114**(18): 183102. https://doi.org/10.1063/1.4829897.
14. Amirmazlaghani, M., Raissi, F., Habibpour, O., et al. (2013). Graphene-Si Schottky IR Detector. IEEE J. Quant. Electron. **49**(7): 589–594. https://doi.org/10.1109/jqe.2013.2261472.
15. Casalino, M. (2019). Silicon Meets Graphene for a New Family of Near-Infrared Schottky Photodetectors. Appl. Sci. **9**(18): 3677. https://doi.org/10.3390/app9183677.
16. Li, X., Chen, X., Li, S., et al. (2021). High performance sub-bandgap photodetection via internal photoemission based on ideal metal/2D-material van der Waals Schottky interface. Nanoscale **13**(39): 16448–16456. https://doi.org/10.1039/d1nr04770a.
17. Wang, F., Zhang, T., Xie, R., et al. (2023). How to characterize figures of merit of two-dimensional photodetectors. Nat. Commun. **14**(1): 2224. https://doi.org/10.1038/s41467-023-37635-1.
18. Lee, S.-J., Cheng, H.-C., Wang, Y., et al. (2023). Lead halide perovskite sensitized WSe2 photodiodes with ultrahigh open circuit voltages. eLight **3**(1): 8. https://doi.org/10.1186/s43593-023-00040-8.
19. Guo, Z., Zeng, Y., Meng, F., et al. (2022). In-situ neutron-transmutation for substitutional doping in 2D layered indium selenide based phototransistor. eLight **2**(1): 9. https://doi.org/10.1186/s43593-022-00017-z.
20. Jiang, H., Wei, J., Sun, F., et al. (2022). Enhanced Photogating Effect in Graphene Photodetectors via Potential Fluctuation Engineering. ACS Nano **16**(3): 4458–4466. https://doi.org/10.1021/acsnano.1c10795.
21. Wei, J., Xu, C., Dong, B., et al. (2021). Mid-infrared semimetal polarization detectors with configurable polarity transition. Nat. Photonics **15**(8): 614–621. https://doi.org/10.1038/s41566-021-00819-6.
22. Zhan, H.E., Xiao-dong, W.E.I., Chun-feng, C.A.I., et al. (2010). PbTe thin film mid-infrared photoconductive detectors grown by molecular beam epitaxy. Infrared Laser Eng. **39**(1): 22–25.
23. Wang, X.-J., Zou, L., Li, D., et al. (2015). Photo-Induced Doping in Graphene/Silicon Heterostructures. J. Phys. Chem. **119**(2): 1061–1066. https://doi.org/10.1021/jp509878m.
24. Ju, L., Velasco, J., Jr., Huang, E., et al. (2014). Photoinduced doping in heterostructures of graphene and boron nitride. Nat. Nanotechnol. **9**(5): 348–352. https://doi.org/10.1038/nnano.2014.60.
25. An, X., Liu, F., Jung, Y.J., et al. (2013). Tunable graphene-silicon heterojunctions for ultrasensitive photodetection. Nano Lett. **13**(3): 909–916. https://doi.org/10.1021/nl303682j.
26. Tang, Y., Li, R., Sun, R., et al. (2023). Flexible all-organic photodetectors via universal water-assisted transfer printing. Innovation **4**(4): 100460. https://doi.org/10.1016/j.xinn.2023.100460.
27. Chen, C.K., Nechay, B., and Tsaur, B.Y. (1991). Ultraviolet, Visible, and Infrared Response of PtSi Schottky-Barrier Detectors Operated in the Front-illuminated Mode. IEEE Trans. Electron. Dev. **38**(5): 1094–1103. https://doi.org/10.1109/16.78384.
28. Wu, J.H., Chang, R.S., and Horng, G.J. (2004). Microstructure, electrical, and optical properties of evaporated PtSi/p-Si(100) Schottky barriers as high quantum efficient infrared detectors. Thin Solid Films **466**(1–2): 314–319. https://doi.org/10.1016/j.tsf.2004.03.016.

29. Wang, F., Liu, Z., Zhang, T., et al. (2022). Fully Depleted Self-Aligned Heterosandwiched Van Der Waals Photodetectors. Adv. Mater. ***34***(39): e2203283. https://doi.org/10.1002/adma.202203283.
30. Wang, F., Zhang, T., Xie, R., et al. (2024). Next-generation Photodetectors Beyond van der Waals Junctions. Adv. Mater. ***36***: e2301197. https://doi.org/10.1002/adma.202301197.
31. Li, C., Wang, H., Wang, F., et al. (2020). Ultrafast and broadband photodetectors based on a perovskite/organic bulk heterojunction for large-dynamic-range imaging. Light Sci. Appl. ***9***: 31. https://doi.org/10.1038/s41377-020-0264-5.
32. Wang, H., Li, Z., Li, D., et al. (2021). Junction Field-Effect Transistors Based on PdSe2/MoS2 Heterostructures for Photodetectors Showing High Responsivity and Detectivity. Adv. Funct. Mater. ***31***(49): 2106105. https://doi.org/10.1002/adfm.202106105.
33. Hu, W., Ye, Z., Liao, L., et al. (2014). 128x128 long-wavelength/mid-wavelength two-color HgCdTe infrared focal plane array detector with ultralow spectral cross talk. Opt. Lett. ***39***(17): 5184–5187. https://doi.org/10.1364/OL.39.005184.
34. Hu, W.D., Chen, X.S., Ye, Z.H., et al. (2011). A hybrid surface passivation on HgCdTe long wave infrared detector with in-situ CdTe deposition and high-density hydrogen plasma modification. Appl. Phys. Lett. ***99***(9): 091101. https://doi.org/10.1063/1.3633103.
35. Xiang, D., Han, C., Hu, Z., et al. (2015). Surface Transfer Doping-Induced, High-Performance Graphene/Silicon Schottky Junction-Based, Self-Powered Photodetector. Small ***11***(37): 4829–4836. https://doi.org/10.1002/smll.201501298.
36. Xu, A., Yang, S., Liu, Z., et al. (2018). Near-infrared photodetector based on Schottky junctions of monolayer graphene/GeOI. Mater. Lett. ***227***: 17–20. https://doi.org/10.1016/j.matlet.2018.04.107.
37. Yu, T., Wang, F., Xu, Y., et al. (2016). Graphene Coupled with Silicon Quantum Dots for High-Performance Bulk-Silicon-Based Schottky-Junction Photodetectors. Adv. Mater. ***28***(24): 4912–4919. https://doi.org/10.1002/adma.201506140.
38. Riazimehr, S., Kataria, S., Bornemann, R., et al. (2017). High Photocurrent in Gated Graphene-Silicon Hybrid Photodiodes. ACS Photonics ***4***(6): 1506–1514. https://doi.org/10.1021/acsphotonics.7b00285.
39. Casalino, M., Russo, R., Russo, C., et al. (2018). Free-Space Schottky Graphene/Silicon Photodetectors Operating at 2 um. ACS Photonics ***5***(11): 4577–4585. https://doi.org/10.1021/acsphotonics.8b01037.
40. Kim, J.W., Kim, C.Y., Kim, J.H., et al. (2021). Highly responsive near-infrared photodetector with low dark current using graphene/germanium Schottky junction with Al2O3 interfacial layer. Pathogens ***10***(5): 1573–1579. https://doi.org/10.1515/nanoph-2021-0002.
41. Kim, W., Arpiainen, S., Xue, H., et al. (2018). Photoresponse of Graphene-Gated Graphene-GaSe Heterojunction Devices. ACS Appl. Nano Mater. ***1***(8): 3895–3902. https://doi.org/10.1021/acsanm.8b00684.
42. Xu, J., Liu, T., Hu, H., et al. (2020). Design and optimization of tunneling photodetectors based on graphene/Al2O3/silicon heterostructures. Nanophotonics ***9***(12): 3841–3848. https://doi.org/10.1515/nanoph-2019-0499.
43. Won, U.Y., Lee, B.H., Kim, Y.R., et al. (2020). Efficient photovoltaic effect in graphene/h-BN/silicon heterostructure self-powered photodetector. Nano Res. ***14***(6): 1967–1972. https://doi.org/10.1007/s12274-020-2866-x.
44. Tang, X., Chen, M., Kamath, A., et al. (2020). Colloidal Quantum-Dots/Graphene/Silicon Dual-Channel Detection of Visible Light and Short-Wave Infrared. ACS Photonics ***7***(5): 1117–1121. https://doi.org/10.1021/acsphotonics.0c00247.
45. Pospischil, A., Humer, M., Furchi, M.M., et al. (2013). CMOS-compatible graphene photodetector covering all optical communication bands. Nat. Photonics ***7***(11): 892–896. https://doi.org/10.1038/nphoton.2013.240.
46. Furchi, M., Urich, A., Pospischil, A., et al. (2012). Microcavity-integrated graphene photodetector. Nano Lett. ***12***(6): 2773–2777. https://doi.org/10.1021/nl204512x.
47. Lemme, M.C., Koppens, F.H.L., Falk, A.L., et al. (2011). Gate-activated photoresponse in a graphene p-n junction. Nano Lett. ***11***(10): 4134–4137. https://doi.org/10.1021/nl2019068.
48. Kim, C.O., Kim, S., Shin, D.H., et al. (2014). High photoresponsivity in an all-graphene p-n vertical junction photodetector. Nat. Commun. ***5***: 3249. https://doi.org/10.1038/ncomms4249.
49. An, Y., Behnam, A., Pop, E., et al. (2013). Metal-semiconductor-metal photodetectors based on graphene/p-type silicon Schottky junctions. Appl. Phys. Lett. ***102***(1): 013110. https://doi.org/10.1063/1.4773992.
50. Xia, F., Mueller, T., Lin, Y.M., et al. (2009). Ultrafast graphene photodetector. Nat. Nanotechnol. ***4***(12): 839–843. https://doi.org/10.1038/nnano.2009.292.
51. Mueller, T., Xia, F., and Avouris, P. (2010). Graphene photodetectors for high-speed optical communications. Nat. Photonics ***4***(5): 297–301. https://doi.org/10.1038/nphoton.2010.40.
52. Li, X., Zhu, M., Du, M., et al. (2016). High Detectivity Graphene-Silicon Heterojunction Photodetector. Small ***12***(5): 595–601. https://doi.org/10.1002/smll.201502336.
53. Almeida, J.M., Wisniowski, P., and Freitas, P.P. (2008). Low-Frequency Noise in MgO Magnetic Tunnel Junctions: Hooge's Parameter Dependence on Bias Voltage. IEEE Trans. Magn. ***44***(11): 2569–2572. https://doi.org/10.1109/tmag.2008.2002604.
54. Wu, P., Ye, L., Tong, L., et al. (2022). Van der Waals two-color infrared photodetector. Light Sci. Appl. ***11***(1): 6. https://doi.org/10.1038/s41377-021-00694-4.
55. Chen, Y., Wang, Y., Wang, Z., et al. (2021). Unipolar barrier photodetectors based on van der Waals heterostructures. Nat. Electron. ***4***(5): 357–363. https://doi.org/10.1038/s41928-021-00586-w.
56. Zou, X., Xu, Y., and Duan, W. (2021). 2D materials: Rising star for future applications. Innovation ***2***(2): 100115. https://doi.org/10.1016/j.xinn.2021.100115.
57. Wei, J., Chen, Y., Li, Y., et al. (2022). Geometric filterless photodetectors for mid-infrared spin light. Nat. Photonics ***17***(2): 171–178. https://doi.org/10.1038/s41566-022-01115-7.
58. Guo, Z., Zhang, Z., Yan, R., et al. (2022). Electrochemical epitaxial PbTe nanowires photodetector for NIR response. Nanotechnology ***33***(48): 485202. https://doi.org/10.1088/1361-6528/ac8b17.

ACKNOWLEDGMENTS

This work was supported by the National Key R&D Program of China (2017YFE0131900), the Natural Science Foundation of Chongqing, China (cstc2019jcyjjqX0017), and the National Natural Science Foundation of China (62204242, 62005182).

AUTHOR CONTRIBUTIONS

J.F. and X.W. conceived the study. J.F. carried out the experiments, including device fabrication, device simulation, and performance characterization, with the help of Z.G., G.L., C.N., and F.S. Z.G. and S.F. promoted the growth of PbTe. J.F. and W.X. performed the analytical analysis. J.F. and X.W. wrote the manuscript with comments from all the other authors. X.W. supervised the project.

DECLARATION OF INTERESTS

The authors declare no competing interests.

SUPPLEMENTAL INFORMATION

It can be found online at https://doi.org/10.1016/j.xinn.2024.100600.

LEAD CONTACT WEBSITE

http://sourcedb.cigit.cas.cn/rcdw/202012/t20201225_5842661.html.